

Geophysical Research Letters[®]

RESEARCH LETTER

10.1029/2021GL097598

Key Points:

- The spatial inhomogeneity of global ocean thermohaline properties has increased over the past decades
- The increase is primarily caused by anthropogenic forcing and is projected to accelerate in the future
- Upper-ocean warming and amplified salinity contrast between the subtropics and subpolar regions dominate the inhomogeneity increase

Supporting Information:

Supporting Information may be found in the online version of this article.

Correspondence to:

Q. Ren,
renqipung@qdio.ac.cn

Citation:

Ren, Q., Kwon, Y.-O., Yang, J., Huang, R. X., Li, Y., & Wang, F. (2022). Increasing inhomogeneity of the global oceans. *Geophysical Research Letters*, *49*, e2021GL097598. <https://doi.org/10.1029/2021GL097598>

Received 21 DEC 2021
Accepted 14 APR 2022

Increasing Inhomogeneity of the Global Oceans

Qiping Ren^{1,2} , Young-Oh Kwon³ , Jiayan Yang³ , Rui Xin Huang³ , Yuanlong Li^{1,4,5}, and Fan Wang^{1,2,4,5} 

¹CAS Key Laboratory of Ocean Circulation and Waves, Institute of Oceanology, Chinese Academy of Sciences, Qingdao, China, ²University of Chinese Academy of Sciences, Beijing, China, ³Woods Hole Oceanographic Institution, Woods Hole, MA, USA, ⁴Center for Ocean Mega-Science, Chinese Academy of Sciences, Qingdao, China, ⁵Function Laboratory for Ocean Dynamics and Climate, Qingdao National Laboratory for Marine Science and Technology, Qingdao, China

Abstract The ocean is inhomogeneous in hydrographic properties with diverse water masses. Yet, how this inhomogeneity has evolved in a rapidly changing climate has not been investigated. Using multiple observational and reanalysis datasets, we show that the spatial standard deviation (SSD) of the global ocean has increased by $1.4 \pm 0.1\%$ in temperature and $1.5 \pm 0.1\%$ in salinity since 1960. A newly defined thermohaline inhomogeneity index, a holistic measure of both temperature and salinity changes, has increased by $2.4 \pm 0.1\%$. Climate model simulations suggest that the observed ocean inhomogeneity increase is dominated by anthropogenic forcing and projected to accelerate by 200%–300% during 2015–2100. Geographically, the rapid upper-ocean warming at mid-to-low latitudes dominates the temperature inhomogeneity increase, while the increasing salinity inhomogeneity is mainly due to the amplified salinity contrast between the subtropical and subpolar latitudes.

Plain Language Summary The ocean's inhomogeneity, quantified by the spatial standard deviation (SSD) of the global water mass, is closely linked to the global ocean's physical and biogeochemical processes. Although previous studies have reported various aspects of the long-term ocean changes, the change of the global ocean inhomogeneity as an integral measure of the water-mass diversity remains unknown. Our study shows that the overall inhomogeneity has increased by $1.4 \pm 0.1\%$ in temperature and $1.5 \pm 0.1\%$ in salinity since 1960. The observed ocean inhomogeneity increase is attributed to anthropogenic forcing and projected to accelerate in the future. The increase in temperature inhomogeneity is mainly due to the rapid upper-ocean warming at mid-to-low latitudes. The amplified salinity contrast between the subtropical and subpolar latitudes contributes to the salinity inhomogeneity increase.

1. Introduction

The ocean is intrinsically inhomogeneous in temperature and salinity. This inhomogeneity fundamentally influences physical and biogeochemical processes of oceans (e.g., DeVries et al., 2017; Fu et al., 2016), causing mixing of water masses, shaping three-dimensional geostrophic circulations through the thermal-wind relation (e.g., Talley, 2008), and giving rise to overturning circulations that regulate the global climate through heat and freshwater transports (e.g., Broecker, 1987; Rintoul, 2018). The ocean inhomogeneity ultimately determines marine biodistribution, ecosystem structure and functioning (Wernberg et al., 2013), and marine biodiversity. With these regards, it is imperative to properly quantify the global ocean inhomogeneity and explore how it has evolved in a changing climate.

Recently, there have been renewed interests in spatial patterns of climate change. Owing to nonuniform radiative forcing and heat redistribution, ocean heat uptake is geographically uneven with some regions exhibiting enhanced warming trends while others experiencing significant cooling trends (Johnson & Lyman, 2020), such as the asymmetric warming trends between the Southern and Northern Hemispheres (Rathore et al., 2020). The global hydrological cycle has strengthened in response to greenhouse-gas warming (e.g., Allan et al., 2014), resulting in amplified geographical salinity contrasts in a so-called “salty gets saltier, fresh gets fresher” pattern (e.g., Durack et al., 2010). These changes in oceans have been linked to extreme climate events, such as marine heat waves (e.g., Holbrook et al., 2019; Marin et al., 2021; Oliver et al., 2021) and cold spells, with adverse consequences to marine ecosystems (e.g., Kerr, 2011; Wernberg et al., 2013, 2016).

How the changing climate affects ocean inhomogeneity is difficult to fathom. The “salty gets saltier, fresh gets fresher” pattern may enhance the global ocean inhomogeneity, whereas the overall decrease in meridional surface temperature gradient due to the Arctic amplification (e.g., Cohen et al., 2014; Holland & Bitz, 2003; Meredith et al., 2019) may reduce the inhomogeneity. In this study, we introduce a robust measure to quantify the global ocean inhomogeneity and its spatial-temporal changes and unravel the underlying processes. The rest of the paper is structured as follows. Section 2 introduces data and methods used in our study. Section 3 describes the time evolution of global ocean inhomogeneity and explores the underlying processes. We will summarize and discuss our findings in Section 4.

2. Data and Methods

2.1. Datasets

We utilize five global observational datasets of ocean temperature (T) and salinity (S) with $1^\circ \times 1^\circ$ horizontal resolution: the gridded Argo data product during 2001–2018 (Hosoda et al., 2009); the Institute of Atmospheric Physics (IAP) ocean analysis during 1960–2019 (Cheng et al., 2020); the Ishii data during 1960–2018 (Ishii et al., 2017); the EN4.2.0 during 1960–2016 (Good et al., 2013); the pentad mean World Ocean Atlas 2018 (WOA18) during 1960–2015 (Locarnini et al., 2019; Zweng et al., 2019). In addition, two ocean reanalysis products for the full-depth ocean are used: the $0.5^\circ \times 0.5^\circ$ SODA2.2.4 for 1960–2010 (Smith et al., 1992); and the $1^\circ \times 1^\circ$ ORAS4 for 1960–2017 (Balmaseda et al., 2013). It is worthy to mention that the data after 2005 are far more reliable than those before due to the advent of Argo. The detailed information for these datasets is listed in Table S1 in Supporting Information S1.

Spatial-temporal changes of global climate arise from a combination of anthropogenic forcing, solar and volcanic forcing, and internal climate variability (Wills et al., 2018). To determine the relative roles of external forcing and internal variability, we used 37 models of Coupled Model Intercomparison Project Phase 6 (CMIP6) historical simulations (1850–2014) and 13 projection simulations under the Shared Socioeconomic Pathways (SSP) 2–4.5, which is a scenario combining SSP2-based socioeconomic and RCP4.5-based energy-emissions-land use scenarios (2015–2100) (Eyring et al., 2016; O'Neill et al., 2016; Table S2 in Supporting Information S1). The multi-model mean (MMM) represents the externally forced variability, while the inter-model spread represents internal climate variability and model structural difference.

These data products cover different periods with different spatial and temporal resolutions. All the original data were interpolated onto $1^\circ \times 1^\circ$ horizontal grids and same depth levels. They are 2-year low-pass filtered using a Hanning-window filter and anomalies are relative to the 1960–1980 baseline (Argo are relative to a 1960–1980 average of IAP) (Supplementary Note 1 for further details of data processing and analyses).

2.2. The Spatial Standard Deviation (SSD)

To quantify the spatial inhomogeneity of a property A , such as T and S , we compute its 3-dimensional volume-weighted SSD (SSD_A) over a target region/depth range as follow:

$$SSD_A(t) = \sqrt{\frac{n}{(n-1) \sum_{x,y,z} w(x,y,z)} \sum_{x,y,z} \left\{ \left[A(x,y,z,t) - \bar{A}(t) \right]^2 w(x,y,z) \right\}} \quad (1)$$

where x , y , z , and t represent longitude, latitude, depth, and time, respectively, w is the volume at a given grid point (x, y, z) that is in the space center, which is used as the weight for averaging, n is the number of grid points in the target region/depth range, and \sum indicates the spatial summation over the target region/depth range. \bar{A} represents the volume-weighted spatial averaged value of A ,

$$\bar{A}(t) = \frac{\sum_{x,y,z} A(x,y,z,t)w(x,y,z)}{\sum_{x,y,z} w(x,y,z)} \quad (2)$$

$SSD_A = 0$ indicates that property A is spatially homogeneous. Here, the target region/depth range for the global volume-weighted SSD spans 0° - 360° E, 70° S- 70° N (the Arctic Ocean is excluded), and the upper 2000 m. The global SSD measures the integral degree of dispersion relative to the global-mean value at a given time.

There exist large spatial spreads for the deviation from the global-mean value, implying the spatially diverse contribution to global ocean inhomogeneity. For the water column at a given horizontal grid point (X, Y) , the “local” SSD relative to the global-mean value \bar{A} is defined as

$$SSD_{A,XY}(X, Y, t) = \sqrt{\frac{n}{(n-1) \sum_z w(X, Y, z)} \sum_z \left\{ \left[A(X, Y, z, t) - \bar{A}(t) \right]^2 w(X, Y, z) \right\}} \quad (3)$$

which represents the contribution of the water column from this geographical location to the global SSD_A . Likewise, for a given layer with a fixed central depth of Z , the “layer” SSD relative to \bar{A} can be expressed as

$$SSD_{A,Z}(Z, t) = \sqrt{\frac{n}{(n-1) \sum_{x,y} w(x, y, Z)} \sum_{x,y} \left\{ \left[A(x, y, Z, t) - \bar{A}(t) \right]^2 w(x, y, Z) \right\}} \quad (4)$$

which represents the contribution of this layer to the global SSD_A . $SSD_{A,XY}(x, y, t)$ and $SSD_{A,Z}(z, t)$ can effectively quantify the relative contribution of water properties at each geographical location and layer to global ocean inhomogeneity, respectively.

2.3. The Thermohaline Inhomogeneity (THI) Index

A new quantity, potential spicity (π), is a fundamental thermodynamic variable that is orthogonal to potential density (σ), providing important thermohaline information independent and supplementary to potential density (Huang et al., 2018; Supplementary Note 2). Potential density and potential spicity share the same unit and have equal weight in quantifying the climate variations, which can be used to quantify the overall ocean thermohaline changes together (Huang, 2020; Huang et al., 2018). In σ - π space (Figure S1a in Supporting Information S1; Huang et al., 2018; Huang, 2020), we propose the THI index to represent the combined effects of temperature and salinity on the global ocean inhomogeneity. THI index is defined as the volume-weighted root-mean-square water mass distance (Huang, 2020; Huang et al., 2018) as follows:

$$THI(t) = \sqrt{\frac{\sum_{x,y,z} [D(x, y, z, t)]^2 w(x, y, z)}{\sum_{x,y,z} w(x, y, z)}} \quad (5)$$

Here, D is the water mass distance in σ - π space and is defined as follows:

$$D(x, y, z, t) = \sqrt{(\sigma_1(x, y, z, t) - \bar{\sigma}_1(t))^2 + (\pi_1(x, y, z, t) - \bar{\pi}_1(t))^2}, \quad (6)$$

where σ_1 and π_1 are potential density and potential spicity relative to 1000 dbar reference level since we are focused on the upper 2000 m. $\bar{\sigma}_1$ and $\bar{\pi}_1$ are the global-mean potential density and potential spicity. The full-depth global THI index is also calculated using σ_1 and π_1 . D represents the deviation of water thermohaline property from the global mean. The smaller the water mass distance, the more similar the water parcel's thermohaline property is to the global mean property (Figures S1b and S1c in Supporting Information S1). Therefore, THI index has the same statistical meaning as global SSD of a single variable, but represent the overall combined thermohaline information, and thus acts as a comprehensive measure for global water mass thermohaline property inhomogeneity.

3. Results

3.1. Increasing Inhomogeneity

The SSD of global ocean temperature (SSD_T) in 0–2000 m derived from multiple observational and reanalysis datasets uniformly exhibit a persistent upward trend since the mid-20th century (Figure 1a). The ensemble mean of

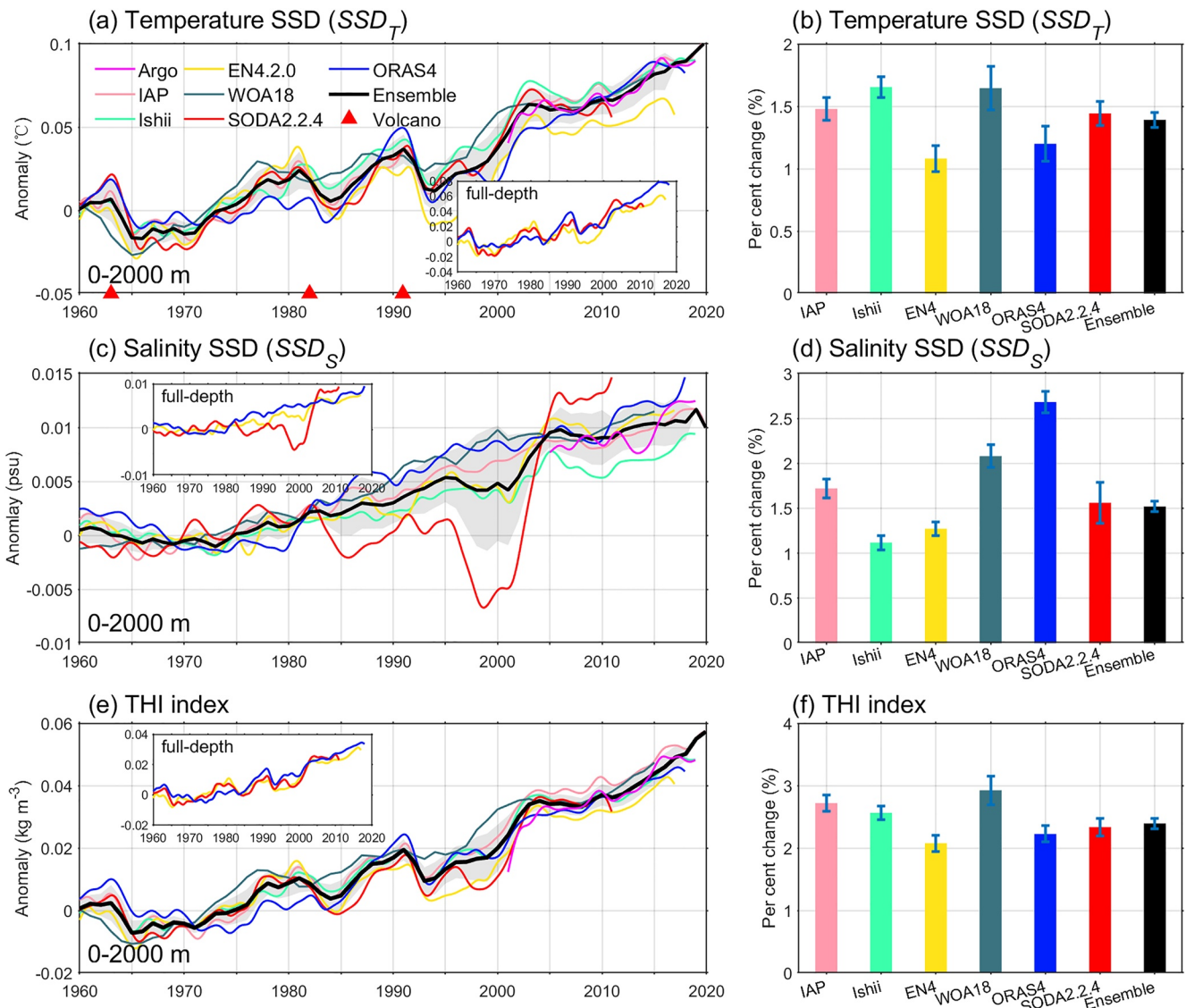


Figure 1. (a) Changes of the 3-dimensional volume-weighted spatial standard deviation (SSD) of global ocean temperature (SSD_T ; unit in $^{\circ}\text{C}$) for 0–2000 m derived from Argo, IAP, Ishii, EN4.2.0, WOA18, SODA2.2.4, and ORAS4. The black thick curve and the gray shading denote the ensemble-mean and one standard deviation range of the 7 datasets, respectively. The inset shows evolutions for the full-depth SSD_T (from the surface to bottom) from EN4.2.0, SODA2.2.4, and ORAS4. Here SSD_T is shown as a 2-year low-pass filtered anomaly relative to the 1960–1980 average baseline (anomaly of Argo is relative to the 1960–1980 average of IAP). The red triangles denote major volcanic eruptions. (b) Percent change of 0–2000 m SSD_T in 1960–2010 relative to the 1960–1980 average value. The error bars denote the 95% confidence interval. (c), (d) and (e), (f) are the same as (a), (b), but for the salinity SSD (SSD_S ; unit in psu) and the thermohaline inhomogeneity (THI) index (kg m^{-3}), respectively.

all datasets yields a baseline value of 5.36°C for 1960–1980 and a trend of $0.015 \pm 0.001^{\circ}\text{C decade}^{-1}$ throughout 1960–2010 that indicates an increase of $1.4 \pm 0.1\%$ (Figure 1b). There were several temporary decreases of global SSD_T following major volcanic eruptions of the 1963 Mount Agung, 1982 El Chichón and 1991 Mount Pinatubo (Figure 1a). Against a backdrop of anthropogenic warming, volcanic eruptions temporarily cooled the surface temperature (Gleckler et al., 2016), reduced the vertical temperature difference that is the main component for the SSD_T (figure not shown), and thus eased the upward trend in SSD_T . Ocean surface warming is likely an important contributor to the temperature inhomogeneity increase.

These datasets also suggest a robust increase in the 0–2000 m salinity SSD (SSD_S) (Figure 1c). The ensemble-mean value of SSD_S during 1960–1980 is 0.64 psu. Based on the mean value, SSD_S has increased by $1.5 \pm 0.1\%$ by 2010 (Figure 1d), corresponding to an upward trend of $2.0 \pm 0.1 \times 10^{-3}$ psu decade^{-1} during 1960–2010. Note

that the global SSD_s is similar to the Salinity Contrast (SC) index proposed by Cheng et al. (2020), defined as the difference between high- and low-salinity regions. The substantial increases in both SSD_s and SC are likely linked to the amplification of climatological salinity patterns in a warming climate (e.g., Cheng et al., 2020). In accordance with the increasing inhomogeneity in both temperature and salinity, similar increases are seen in the inhomogeneity of potential density and potential spicity (Figure S2 in Supporting Information S1).

As a holistic measure of water mass thermohaline inhomogeneity, the global THI index has also increased at an ensemble-mean rate of $8.0 \pm 0.3 \times 10^{-3} \text{ kg m}^{-3} \text{ decade}^{-1}$ since 1960 (Figure 1e), yielding a total increase of $2.4 \pm 0.1\%$ by 2010 relative to the 1960–1980 mean value of 1.72 kg m^{-3} (Figure 1f). Note that changes in the THI index are larger than those of SSD_T and SSD_s , owing to nonlinearity. The contribution from temperature to THI index increase is much larger than salinity (Supplementary Note 3), $8.2(\pm 0.5) \times 10^{-3}$ versus $1.3(\pm 0.3) \times 10^{-3} \text{ kg m}^{-3} \text{ decade}^{-1}$ (Figure S3 in Supporting Information S1). We also computed these measures for the full-depth ocean using a subset of the datasets and obtained similar results (insets in Figure 1). The full-depth ocean inhomogeneity increase is weaker in magnitude than that of 0–2000 m (by 60% for SSD_T , 42% for SSD_s , and 52% for THI index), consistent with the stronger spatial variations in the upper ocean (Rathore et al., 2020).

3.2. Cause of the Increasing Inhomogeneity

The ongoing anthropogenic warming has resulted in robust temperature and salinity changes (e.g., Johnson & Lyman, 2020; Rathore et al., 2020; Durack et al., 2010) and thereby altered ocean inhomogeneity. We compare the ensemble-mean changes in SSD and THI index from observational and reanalysis datasets (collectively addressed as “observation” hereafter) and CMIP6 historical simulations to examine whether the observed inhomogeneity increase arises from natural variability or anthropogenic forcing. Albeit with large inter-model spreads due to internal climate variability and structural differences among models (Plesca et al., 2018), the MMM of 37 CMIP6 historical simulations well reproduces the observed increases in SSD_T , SSD_s , and THI index (Figures 2a–2c). In particular, the linear trends of SSD_T and THI index during 1960–2014 from the CMIP6 historical MMM are statistically indistinguishable from the observed trends at 95% level (insets in Figures 2a and 2c). This consistency between observation and CMIP6 MMM points to anthropogenic forcing, rather than internal variability, as the dominant driver of the increasing ocean inhomogeneity. However, the simulated long-term increases of SSD_s during 1960–2014 in CMIP6 historical MMM are weaker than those in observation, and the difference is statistically significant (inset in Figure 2b). The global SSD_s trend diagnosed from CMIP6 MMM accounts for only ~60% of the observed trend. This could be related to model biases in the simulated subsurface salinity changes (Durack et al., 2012). Besides, the internal variability, which is mostly canceled out in the CMIP6 MMM by definition, may also cause the observation-model discrepancy. As in Figure 1, signatures of volcanic effects, characterized by temporary drops, are discernible in SSD_T and THI index (Figures 2a and 2c), suggesting that the short-lived natural radiative forcing operates in the same way as the long-term anthropogenic forcing for ocean inhomogeneity.

Projections by climate models provide an assessment of whether the increase in ocean inhomogeneity would continue in the future. Based on CMIP6 simulations under the SSP2-4.5 future scenario, the global SSD_T and SSD_s , as well as THI index, are all projected to further increase in the 21st century, and the trends are greater by 2–3 folds than those observed in 1960–2014 (insets in Figures 2a–2c). By 2100, the SSD_T , SSD_s , and THI index would be increased by $7.7 \pm 0.4\%$, $5.8 \pm 0.2\%$, and $13.3 \pm 0.4\%$, respectively, relative to 1960–1980.

The inter-model spread is used to further understand the ocean inhomogeneity change. All CMIP6 models show a significant warming trend in the global mean sea surface temperature (GMSST), accompanying the overall increasing SSD_T with a large spread (Figure 2d). There is a clear inter-model correspondence between the surface warming trends and the SSD_T increase; the inter-model correlation is 0.79, significant at 99.5% level. This result further supports our inference hereinbefore that the surface warming under anthropogenic forcing is the primary cause for ocean temperature inhomogeneity increase.

We further explore the inter-model relationship between the changes in global salinity inhomogeneity and salinity pattern (Figure 2e). In observation, the surface salinity change pattern is approximately consistent with that of the 0–2000 m average salinity change (Cheng et al., 2020). Here, we use the surface salinity contrast (SSC) as a proxy for the pattern, defined as the surface salinity difference between the saltier subtropical regions (20°–35°N and

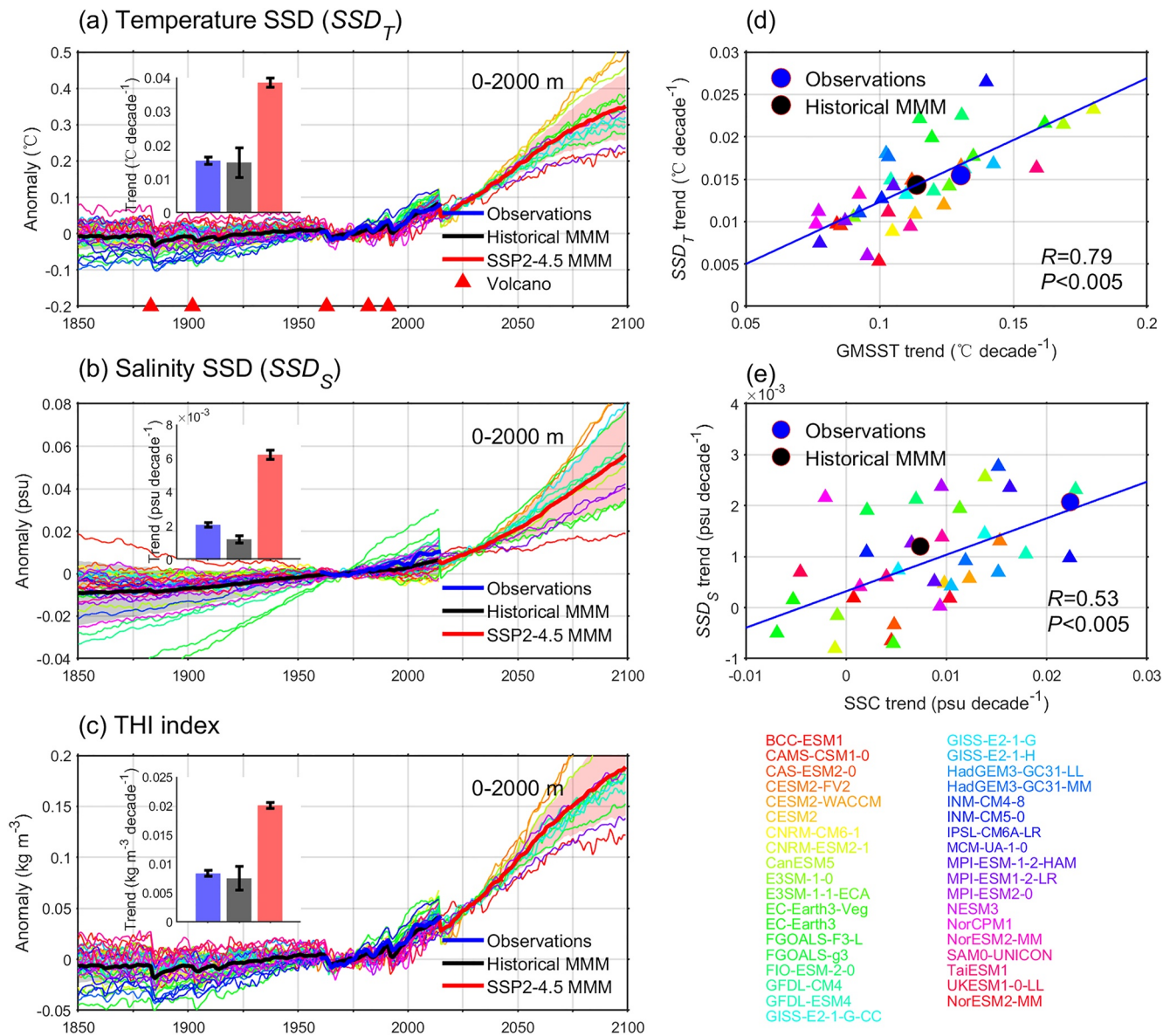


Figure 2. Evolutions of SSD_T (a), SSD_S (b), and THI index (c) of the 0–2000 m global ocean derived from CMIP6 models (37 models for historical simulations of 1850–2014 and 13 models for SSP2-4.5 projections of 2015–2100), shown as the anomalies relative to the 1960–1980 baseline. The multi-model mean (MMM) is plotted as a thick curve (black for 1850–2014 and red for 2015–2100), and their one standard deviation ranges are plotted as the shading. Thick blue curves denote the ensemble mean of observational and reanalysis datasets from Figure 1. The red triangles in a denote the major volcanic eruptions. The inset compares the 1960–2014 linear trend from observations (blue), the 1960–2014 linear trend from CMIP6 historical MMM (black), and the 2015–2100 linear trend from CMIP6 SSP2-4.5 MMM (red), respectively, with the error bars showing 95% confidence intervals. (d) The inter-model relationship between global mean sea-surface temperature (GMSST) trend and 0–2000 m SSD_T trend during 1960–2014. The correlation coefficient R with its p -value and the linear fit (blue solid line) are shown. (e) As in (d), but for the inter-model relationship between the surface salinity contrast (SSC) trend and 0–2000 m SSD_S trend during 1960–2014. The model names are listed in corresponding colors.

20°–30°S) and the fresher subpolar regions (40°–60°N and 40°–60°S) (Figure S4 in Supporting Information S1). The SSC increase indicates amplification of the climatological salinity pattern potentially linked to the strengthening global hydrological cycle. 28 out of 37 CMIP6 models show both an increased SSC and an increased SSD_S during 1960–2014. The inter-model correlation coefficient is 0.53, also significant at 99.5% level. Therefore, the increasing salinity inhomogeneity, to some extent, reflects the amplification of the climatological salinity pattern (e.g., Cheng et al., 2020).

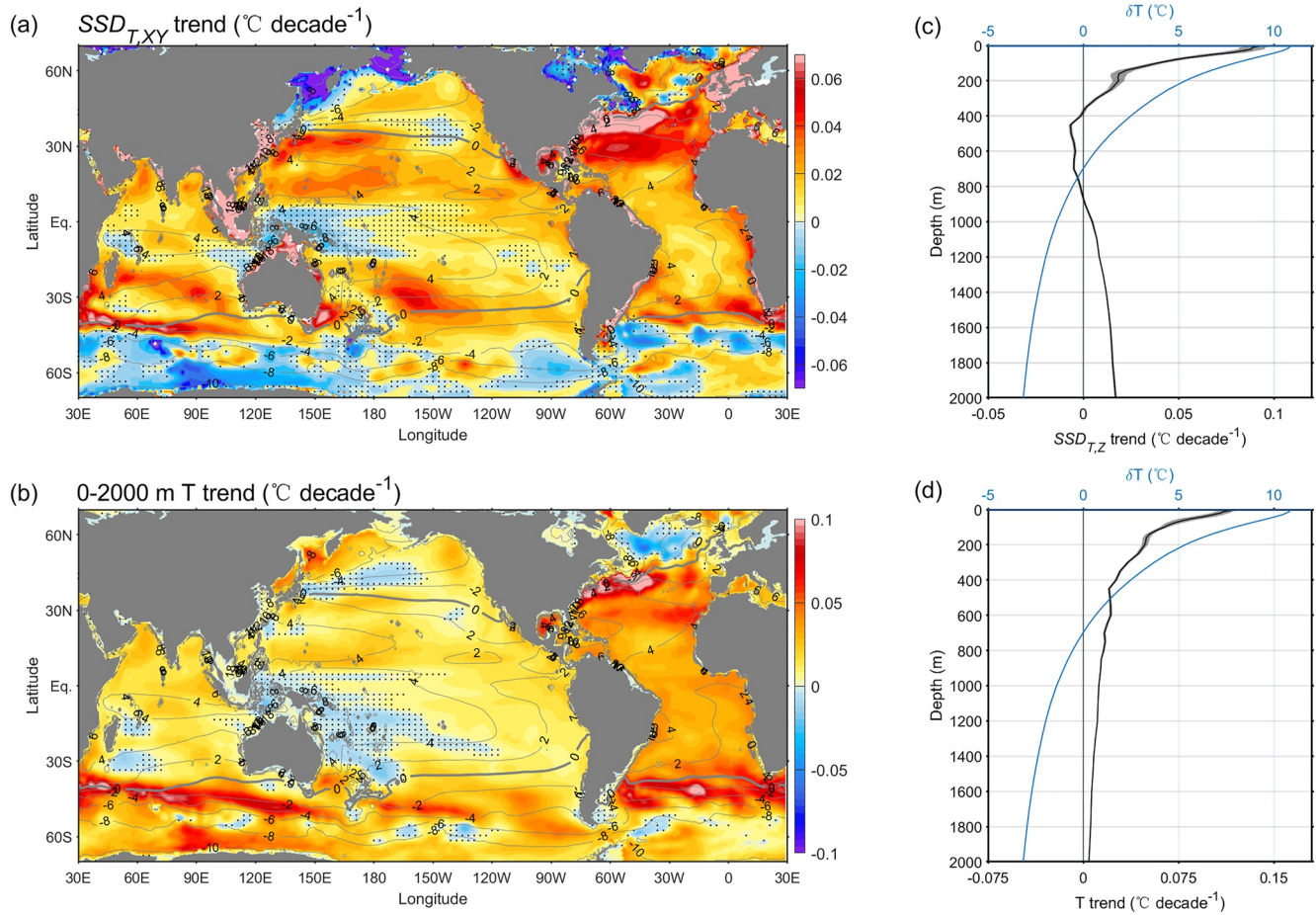


Figure 3. (a) Horizontal distributions of $SSD_{T,XY}$ trend during 1960–2019. (b) As in (a), but for 0–2000 m average temperature trend. Gray contours in a and b show the climatological temperature deviation δT ($^{\circ}\text{C}$) from the global mean temperature for 1960–2019. Stippling indicates the insignificant trends at 95%. (c) Vertical distributions of $SSD_{T,Z}$ trend during 1960–2019. (d) As in (c), but for horizontally averaged temperature trend. The shadings denote the 95% confidence interval. The blue curves in c and d denote the climatological global-mean δT profile. All results are based on IAP data.

3.3. Geographical Distributions

The inhomogeneity change discussed so far is based on the three-dimensional integral measures over the global ocean. To understand the underlying processes, it is instructive to assess the contribution of regions to global inhomogeneity increase and identify potential “hotspots”. First, we use the “local” temperature SSD ($SSD_{T,XY}$) to quantify the regional contribution to global SSD_T . Figure 3a shows the geographical distribution for linear trends of 0–2000 m $SSD_{T,XY}$. More than 90% of the global ocean exhibits significant $SSD_{T,XY}$ increases. In particular, the subtropical gyres show prevailing strong trends with the regional maxima along the subtropical western boundary currents and their extensions, particularly the Gulf Stream. Besides, some local “hotspots” with trends exceeding $0.06^{\circ}\text{C decade}^{-1}$ are concentrated in the shallow marginal seas such as the North Sea and Indonesian Seas. There are also negative contributions, that is, $SSD_{T,XY}$ trends < 0 , from parts of the Southern Ocean and subpolar marginal seas of the Northern Hemisphere.

To understand the $SSD_{T,XY}$ trend pattern, we also plot the climatological temperature deviation (δT) from the global-mean temperature as gray contours in Figures 3a and 3b. There is an overall similarity between the patterns of $SSD_{T,XY}$ trend and climatological δT , both with prevailing positive over mid-to-low latitudes and negative at high latitudes. This pattern indicates that the climatologically warmer region is warming at faster rates (Figure 3b), thus enhancing the global SSD_T . Considering the negative δT , the cooled subpolar North Atlantic also contributes to the global SSD_T increase, while the enhanced warming in the Southern Ocean (Boning et al., 2008; Gille, 2002)

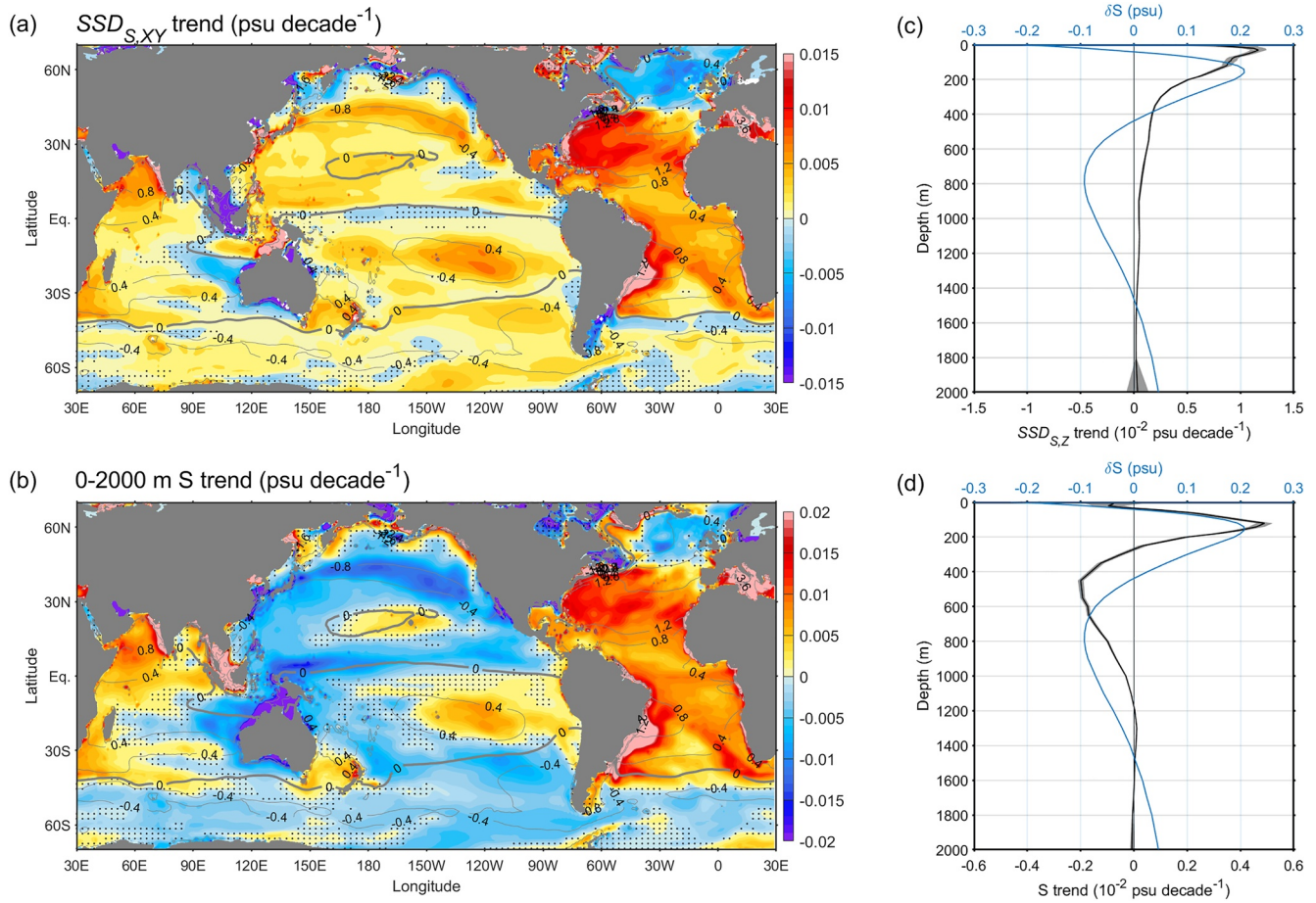


Figure 4. Same as Figure 3, but for horizontal distributions of $SSD_{S,XY}$ trend (a) and 0–2000 m average salinity trend (b), and vertical distributions of $SSD_{S,Z}$ trend (c) and horizontally averaged salinity trend (d). Grey contours in a and b show the climatological salinity deviation δS (psu) from the global mean salinity. The blue curves in c and d denote the climatological global-mean δS profile.

attenuates the spatial temperature contrast and reduces the global SSD_T . The “hotspots” of increasing $SSD_{T,XY}$ in the Gulf Stream are owing to strong local warming trends.

Next, we use the “layer” SSD of temperature ($SSD_{T,Z}$) to examine contributions from different depths. The $SSD_{T,Z}$ change shows a vertical sandwiched structure: strong increasing trends in the upper 400 m with the maximum near the surface, weak decreasing trends between 400 and 800 m, and sizable increasing trends below 800 m (Figure 3c). This vertical structure can be understood again by considering the vertical structure of the climatological δT and the warming trend together (Figure 3d). The strong warming trends in the upper 400 m coincide with the positive δT , thus further warming over the already warmer part enhances the temperature contrast and contributes to $SSD_{T,Z}$ increase. The upper-ocean warming under greenhouse gas forcing leads to rapid warming of global-mean temperature. As a result, the slower warming in the 400–800 m (relative to global-mean warming pace) attenuates the global SSD_T . In the deeper layers (800–2000 m), the warming rates are much slower than the global-mean rate, along with negative δT , contributing positively to global SSD_T increase. These results reveal the importance of the rapid upper-ocean warming over mid-to-low latitudes, particularly in the Atlantic, in the amplification of temperature contrast patterns.

Similar to $SSD_{T,XY}$, the “local” SSD of salinity ($SSD_{S,XY}$) has increased in most areas, and the strongest trends are concentrated in the subtropical Atlantic Ocean especially along the Gulf Stream (Figure 4a). There are salinification trends in the subtropical Pacific and Atlantic and the northern Indian Ocean, and freshening trends in the subpolar North Pacific and the Southern Ocean. These trends act to amplify their climatological δS values (Figure 4b) and lead to $SSD_{S,XY}$ increase. The southern Indian and western Pacific Oceans and the subpolar North

Atlantic are of positive δS values and show freshening trends. However, the freshening in the southern Indo-Pacific Oceans mainly occurs in the low-salinity Antarctic Intermediate Water between 500 and 1200 m (Wong et al., 1999) where δS is negative (Figure 4d), and thus $SSD_{s,XY}$ still increases there.

The “layer” SSD of salinity ($SSD_{s,Z}$) has increased at all depths of 0–2000 m (Figure 4c). Similar to $SSD_{T,Z}$, the $SSD_{s,Z}$ trend is the largest near the surface, which confirms that the larger the depth integral, the weaker the ocean inhomogeneity (Figure 1). The surface $SSD_{s,Z}$ change is probably owing to the spatially inhomogeneous changes in the surface freshwater fluxes associated with the global hydrological cycle change. There is a close resemblance between the vertical structure of δS and salinity trend profiles (Figure 4d). The salinity maximum in the high-salinity subtropical underwaters (100–300 m) and minimum in the low-salinity intermediate waters (500–1000 m) are both strengthened and contribute to global SSD_s increase. Therefore, global SSD_s increase is primarily due to the amplification of the 3-dimensional salinity pattern, which is likely attributed to the strengthening of the global water cycle.

4. Discussion

In this study, we investigate the long-term changes of global ocean inhomogeneity by computing SSD_T , SSD_s , and THI index using multiple datasets and climate model simulations, showing a consensus on the increased global ocean inhomogeneity over the past half-century. The global SSD_T , SSD_s and THI index in 0–2000 m increased by $1.4 \pm 0.1\%$, $1.5 \pm 0.1\%$ and $2.4 \pm 0.1\%$ during 1960–2010 from 1960 to 1980 average, respectively. The global ocean inhomogeneity increase is dominated by anthropogenic forcing and is projected to be accelerated by 2–3 times in the future (insets in Figures 2a–2c). Local SSD trend distributions suggest that global inhomogeneity increase largely results from the amplification of the corresponding climatological contrast patterns. The rapid upper-ocean warming over mid-to-low latitude dominates the SSD_T increase, while the amplification of the salinity pattern, primarily in the subtropical Atlantic, causes increasing SSD_s .

Our quantifications of ocean inhomogeneity provide a novel perspective for understanding the ongoing climate change in oceans. The largest contribution to the global inhomogeneity changes comes from regions of the strongest mean changes (Figures 3 and 4). Changes in inhomogeneity, if continued and amplified in the future, would significantly affect local water mass properties, leading to the formation of new water-mass types (Figure S5 in Supporting Information S1) and extreme climate events such as marine heat waves (e.g., Frölicher et al., 2018; Talley, 2008; Marin et al., 2021; Holbrook et al., 2019; Oliver et al., 2021). The enhanced inhomogeneity may also affect natural climate variability and vice versa, as suggested in Figures 2d and 2e, resulting in changes in the climate variability modes and their inter-basin interactions (Cai et al., 2019; Wang, 2019). It also implies that ocean temperature and salinity under rapid global warming are moving to a new equilibrium climate state with larger hydrographic diversity, posing challenges for future climate prediction.

Global ocean inhomogeneity is intrinsically related to ocean dynamical and thermodynamic processes. A recent study suggested that global mean ocean circulation may be accelerating (Hu et al., 2020). The baroclinic component of large-scale circulations, which are predominantly geostrophic, is directly related to the density variation or the inhomogeneity through the thermal-wind relation. Are circulation acceleration and inhomogeneity increase two faces of the same coin? In addition to the thermohaline changes, inhomogeneities of other water properties, including biogeochemical ones, may have also experienced long-term changes upon the thermodynamic adjustment and need to be examined.

Increase in global inhomogeneity in response to the anthropogenic climate change is a surprising result, especially as some aspects of the climate change seemingly suggest the opposite, for example, weakening of the equator-to-pole surface temperature gradient due to the polar amplification (Holland & Bitz, 2003; Meredith et al., 2019). While our study newly identified the increasing inhomogeneity in the global ocean, how does the anthropogenic climate change drive the increase in the global inhomogeneity needs to be more thoroughly investigated in the future, to obtain a more clear mechanistic understanding of this newly found phenomenon.

Data Availability Statement

The data are available in the following links: Argo (http://www.jamstec.go.jp/ARGO/J_ARGOe.html); IAP (<http://www.ocean.iap.ac.cn/pages/dataService/dataService.html?navAnchor=dataService>); Ishii V7.2 (<https://climate.mri-jma.go.jp/pub/ocean/ts/v7.2/>); EN4.2.0 (<https://www.metoffice.gov.uk/hadobs/en4/>); Pentad WOA18 (https://www.nodc.noaa.gov/OC5/3M_HEAT_CONTENT/); SODA2.2.4 (<http://iridl.ldeo.columbia.edu/SOURCES/.CARTON-GIESE/.SODA/.v2p2p4/>); and ORAS4 (<https://www.ecmwf.int/en/research/climate-reanalysis/ocean-reanalysis/>). The CMIP6 model outputs are available from the World Climate Research Programme (<https://esgf-node.llnl.gov/search/cmip6/>).

Acknowledgments

This work is supported by the Strategic Priority Research Program of Chinese Academy of Sciences (grant XDB42000000 and XDB40000000), the National Key R&D Program of China (2017YFA0603200), and the Shandong Provincial Natural Science Foundation (ZR2020JQ17), and the U.S. National Science Foundation Physical Oceanography Program (OCE- 2048336). We are grateful to Nathan Bindoff and two anonymous reviewers, whose comments helped to improve this manuscript.

References

- Allan, R. P., Liu, C. L., Zahn, M., Lavers, D. A., Koukouvagias, E., Bodas-Salcedo, A., & Vidale, P. L. (2014). Physically consistent responses of the global atmospheric hydrological cycle in models and observations. *Surveys in Geophysics*, 35(3), 533–552. <https://doi.org/10.1002/2014GL060962>
- Balmaseda, M. A., Mogensen, K., & Weaver, A. T. (2013). Evaluation of the ECMWF ocean reanalysis system ORAS4. *Quarterly Journal of the Royal Meteorological Society*, 139(674), 1132–1161. <https://doi.org/10.1002/qj.2063>
- Boning, C. W., Dispert, A., Visbeck, M., Rintoul, S. R., & Schwarzkopf, F. U. (2008). The response of the Antarctic Circumpolar Current to recent climate change. *Nature Geoscience*, 1(12), 864–869. <https://doi.org/10.1038/ngeo362>
- Broecker, W. S. (1987). The biggest chill. *Natural History*, 96(10), 74.
- Cai, W., Wu, L., Lengaigne, M., Li, T., McGregor, S., Kug, J. S., et al. (2019). Panropical climate interactions. *Science*, 363(6430). <https://doi.org/10.1126/science.aav4236>
- Cheng, L., Trenberth, K. E., Gruber, N., Abraham, J. P., Fasullo, J. T., Li, G., et al. (2020). Improved estimates of changes in upper ocean salinity and the hydrological cycle. *Journal of Climate*, 33(23), 10357–10381. <https://doi.org/10.1175/JCLI-D-20-0366.1>
- Cohen, J., Screen, J. A., Furtado, J. C., Barlow, M., Whittleston, D., Coumou, D., et al. (2014). Recent Arctic amplification and extreme mid-latitude weather. *Nature Geoscience*, 7(9), 627–637. <https://doi.org/10.1038/ngeo2234>
- DeVries, T., Holzer, M., & Primeau, F. (2017). Recent increase in oceanic carbon uptake driven by weaker upper-ocean overturning. *Nature*, 542(7640), 215–218. <https://doi.org/10.1038/nature21068>
- Durack, P. J., Wijffels, S. E., & Matear, R. J. (2012). Ocean salinities reveal strong global water cycle intensification during 1950 to 2000. *Science*, 336(6080), 455–458.
- Eyring, V., Bony, S., Meehl, G. A., Senior, C. A., Stevens, B., Stouffer, R. J., & Taylor, K. E. (2016). Overview of the coupled model Inter-comparison Project Phase 6 (CMIP6) experimental design and organization. *Geoscientific Model Development*, 9(5), 1937–1958. <https://doi.org/10.5194/gmd-9-1937-2016>
- Frolicher, T. L., Fischer, E. M., & Gruber, N. (2018). Marine heatwaves under global warming. *Nature*, 560(7718), 360. <https://doi.org/10.1038/s41586-018-0383-9>
- Fu, W. W., Randerson, J. T., & Moore, J. K. (2016). Climate change impacts on net primary production (NPP) and export production (EP) regulated by increasing stratification and phytoplankton community structure in the CMIP5 models. *Biogeosciences*, 13(18), 5151–5170. <https://doi.org/10.5194/bg-13-5151-2016>
- Gille, S. T. (2002). Warming of the Southern Ocean since the 1950s. *Science*, 295(5558), 1275–1277. <https://doi.org/10.1126/science.1065863>
- Gleckler, P. J., Durack, P. J., Stouffer, R. J., Johnson, G. C., & Forest, C. E. (2016). Industrial-era global ocean heat uptake doubles in recent decades. *Nature Climate Change*, 6(4), 394–398. <https://doi.org/10.1038/nclimate2915>
- Good, S. A., Martin, M. J., & Rayner, N. A. (2013). EN4: Quality controlled ocean temperature and salinity profiles and monthly objective analyses with uncertainty estimates. *Journal of Geophysical Research: Oceans*, 118(12), 6704–6716. <https://doi.org/10.1002/2013jc009067>
- Holbrook, N. J., Scannell, H. A., Sen Gupta, A., Benthuyssen, J. A., Feng, M., Oliver, E. C. J., et al. (2019). A global assessment of marine heatwaves and their drivers. *Nature Communications*, 10(1), 2624. ARTN 262410. <https://doi.org/10.1038/s41467-019-10206-z>
- Holland, M. M., & Bitz, C. M. (2003). Polar amplification of climate change in coupled models. *Climate Dynamics*, 21(3–4), 221–232. <https://doi.org/10.1007/s00382-003-0332-6>
- Hosoda, S., Suga, T., Shikama, N., & Mizuno, K. (2009). Global surface layer salinity change detected by Argo and its implication for hydrological cycle intensification. *Journal of Oceanography*, 65(4), 579–586. <https://doi.org/10.1007/s10872-009-0049-1>
- Hu, S., Sprintall, J., Guan, C., McPhaden, M. J., Wang, F., Hu, D., & Cai, W. (2020). Deep-reaching acceleration of global mean ocean circulation over the past two decades. *Science Advances*, 6(6), 1–9. <https://doi.org/10.1126/sciadv.aax7727>
- Huang, R. X. (2020). *Heaving, stretching and spicing modes, climate variability in the ocean*. Higher Education Press and Springer Nature Singapore Pte Ltd. (p. 391).
- Huang, R. X., Yu, L. S., & Zhou, S. Q. (2018). New definition of potential spicity by the least square method. *Journal of Geophysical Research: Oceans*, 123(10), 7351–7365. <https://doi.org/10.1029/2018JC014306>
- Ishii, M., Fukuda, Y., Hirahara, S., Yasui, S., Suzuki, T., & Sato, K. (2017). Accuracy of global upper ocean heat content estimation expected from present observational data sets. *Sola*, 13, 163–167. <https://doi.org/10.2151/sola.2017-030>
- Johnson, G. C., & Lyman, J. M. (2020). Warming trends increasingly dominate global ocean. *Nature Climate Change*, 10(August), 757–761. <https://doi.org/10.1038/s41558-020-0822-0>
- Kerr, R. A. (2011). CLIMATE CHANGE humans are driving extreme weather; time to prepare. *Science*, 334(6059), 1040. <https://doi.org/10.1126/science.334.6059.1040>
- Locarnini, R. A., Mishonov, A. V., Baranova, O. K., Boyer, T. P., Zweng, M. M., Garcia, H. E., et al. (2019). World Ocean Atlas 2018. In In A. Mishonov (Ed.), *Temperature*. Technical Editor, NOAA Atlas NESDIS 81, (Vol. 1, p. 52).
- Marin, M., Feng, M., Phillips, H. E., & Bindoff, N. L. (2021). A global, multiproduct analysis of coastal marine heatwaves: Distribution, characteristics, and long-term trends. *Journal of Geophysical Research: Oceans*, 126(2), ARTN e2020JC016708. <https://doi.org/10.1029/2020JC016708>
- Meredith, M., Sommerkorn, M., Cassotta, S., Derksen, C., Ekaykin, A., Hollowed, A., et al. (2019). Polar regions. In H.-O. Pörtner, D. C. Roberts, V. Masson-Delmotte, P. Zhai, M. Tignor, E. Poloczanska, K. Mintenbeck, A. Alegría, M. Nicolai, A. Okem, J. Petzold, B. Rama, & N. M. Weyer (Eds.), *IPCC special report on the ocean and cryosphere in a changing climate*.

- Oliver, E. C., Benthuisen, J. A., Darmaraki, S., Donat, M. G., Hobday, A. J., Holbrook, N. J., et al. (2021). Marine heatwaves. *Annual Review of Marine Science*, 13(1), 313–342. <https://doi.org/10.1146/annurev-marine-032720-095144>
- O'Neill, B. C., Tebaldi, C., Van Vuuren, D. P., Eyring, V., Friedlingstein, P., Hurtt, G., et al. (2016). The scenario model Intercomparison Project (ScenarioMIP) for CMIP6. *Geoscientific Model Development*, 9(9), 3461–3482. <https://doi.org/10.5194/gmd-9-3461-2016>
- Plesca, E., Grutzun, V., & Buehler, S. A. (2018). How robust is the weakening of the Pacific walker circulation in CMIP5 idealized transient climate simulations? *Journal of Climate*, 31(1), 81–97. <https://doi.org/10.1175/jcli-d-17-0151.1>
- Rathore, S., Bindoff, N. L., Phillips, H. E., & Feng, M. (2020). Recent hemispheric asymmetry in global ocean warming induced by climate change and internal variability. *Nature Communications*, 11(1), 1–8. <https://doi.org/10.1038/s41467-020-15754-3>
- Rintoul, S. R. (2018). The global influence of localized dynamics in the Southern Ocean. *Nature*, 558(7709), 209–218. <https://doi.org/10.1038/s41586-018-0182-3>
- Smith, R. D., Dukowicz, J. K., & Malone, R. C. (1992). Parallel ocean general-circulation modeling. *Physica D: Nonlinear Phenomena*, 60(1–4), 38–61. [https://doi.org/10.1016/0167-2789\(92\)90225-c](https://doi.org/10.1016/0167-2789(92)90225-c)
- Talley, L. D. (2008). Freshwater transport estimates and the global overturning circulation: Shallow, deep and throughflow components. *Progress in Oceanography*, 78(4), 257–303. <https://doi.org/10.1016/j.pocean.2008.05.001>
- Wang, C. (2019). Three-ocean interactions and climate variability: A review and perspective. *Climate Dynamics*, 53(7–8), 5119–5136. <https://doi.org/10.1007/s00382-019-04930-x>
- Wernberg, T., Bennett, S., Babcock, R. C., De Bettignies, T., Cure, K., Depczynski, M., et al. (2016). Climate-driven regime shift of a temperate marine ecosystem. *Science*, 353(6295), 169–172. <https://doi.org/10.1126/science.aad8745>
- Wernberg, T., Smale, D. A., Tuya, F., Thomsen, M. S., Langlois, T. J., De Bettignies, T., et al. (2013). An extreme climatic event alters marine ecosystem structure in a global biodiversity hotspot. *Nature Climate Change*, 3(1), 78–82. <https://doi.org/10.1038/nclimate1627>
- Wills, R. C., Schneider, T., Wallace, J. M., Battisti, D. S., & Hartmann, D. L. (2018). Disentangling global warming, multidecadal variability, and El Niño in Pacific temperatures. *Geophysical Research Letters*, 45(5), 2487–2496. <https://doi.org/10.1002/2017GL076327>
- Wong, A. P. S., Bindoff, N. L., & Church, J. A. (1999). Large-scale freshening of intermediate waters in the Pacific and Indian oceans. *Nature*, 400(6743), 440–443. <https://doi.org/10.1038/22733>
- Zweng, M. M., Seidov, D., Boyer, T., Locarnini, M., Garcia, H., Smolyar, I., et al. (2019). World Ocean Atlas 2018. In A. Mishonov (Ed.), *Salinity* (Vol. 2, p. 50). NOAA Atlas NESDIS 82. Technical Editor.

References From the Supporting Information

- Mamayev, O. I. (1975). *Temperature-salinity analysis of world ocean waters*. Elsevier Scientific Publishing Company. (p. 384).
- Munk, W. (1981). Internal waves and small-scale processes. In *Evolution of physical oceanography* (pp. 264–291). MIT Press.
- Stommel, H. (1962). On the cause of the temperature-salinity curve in the ocean. *National Academy of Science*, 48(5), 764–766. <https://doi.org/10.1073/pnas.48.5.764>
- Veronis, G. (1972). On properties of seawater defined by temperature, salinity and pressure. *Journal of Marine Research*, 30, 227–255.

1

2

Geophysical Research Letters

3

Supporting Information for

4

Increasing Inhomogeneity of the Global Oceans

5

Qiuping Ren^{1,2,*}, Young-Oh Kwon³, Jiayan Yang³, Rui Xin

6

Huang³, Yuanlong Li^{1,4,5}, Fan Wang^{1,2,4,5}

7

¹CAS Key Laboratory of Ocean Circulation and Waves, Institute of Oceanology, Chinese Academy of Sciences, Qingdao, China,

8

9

²University of Chinese Academy of Sciences, Beijing, China,

10

³Woods Hole Oceanographic Institution, Woods Hole, MA, USA,

11

⁴Center for Ocean Mega-Science, Chinese Academy of Sciences, Qingdao, China,

12

⁵Function Laboratory for Ocean Dynamics and Climate, Qingdao National Laboratory for Marine Science and Technology, Qingdao, China,

13

14

Contents of this file

15

Table S1

16

Table S2

17

Supplementary Note1

18

Supplementary Note2

19

Supplementary Note3

20

Figure S1

21

Figure S2

22

Figure S3

23

Figure S4

24

Figure S5

25 **Introduction**

26 Two tables, two notes, and five figures are uploaded as supporting
27 information. *Table S1* shows the detailed information of observational and
28 reanalysis datasets used in this study. *Table S2* shows the CMIP6 models used
29 in this study. *Supplementary Note1* describes the detailed information of
30 statistical analysis in this study. *Supplementary Note2* introduces the potential
31 spicity. *Supplementary Note3* shows the calculation of contributions from the
32 temperature and salinity changes to the THI index. *Figure S1* shows the
33 climatological volumetric distribution of water masses on the σ_1 - π_1 diagram
34 and spatial maps of the water mass distance. *Figure S2* shows the changes in
35 the inhomogeneity of global ocean potential density and potential spicity.
36 *Figure S3* shows the changes in temperature and salinity components of the
37 THI index. *Figure S4* shows the climatological zonal mean surface salinity in
38 CMIP6 models. *Figure S5* shows the climatological volumetric distribution of
39 water masses on θ - S diagram and its changes.

40

41 **Supplementary Tables**

42 **Table S1.** Information of observational and reanalysis datasets used in this study.

Datasets	Time coverage	Resolution			References
		Time	Horizontal	Vertical	
Argo	2001-2018	Monthly	1° × 1°	25 levels (0-2000 m)	Hosoda et al., 2009
IAP	1940-2019	Monthly	1° × 1°	41 levels (0-2000 m)	Cheng et al., 2020
Ishii	1955-2018	Monthly	1° × 1°	24 layers (0-3000 m)	Ishii et al., 2017
EN4.2.0	1950-2016	Monthly	1° × 1°	42 layers (full depth)	Good et al., 2013
WOA18	1955-2015	Pentad	1° × 1°	26 layers (0-2000 m)	Locarnini et al., 2019; Zweng et al., 2019
SODA2.2.4	1940-2010	Monthly	0.5° × 0.5°	40 layers (full depth)	Smith et al., 1992
ORAS4	1958-2017	Monthly	1° × 1°	42 layers (full depth)	Balmaseda et al., 2013

44 **Table S2.** 37 models of Coupled Model Intercomparison Project Phase 6 (CMIP6)
 45 historical simulations and 13 projection simulations under the Shared Socioeconomic
 46 Pathways (SSP) 2-4.5. The historical models are forced with time-varying natural
 47 (solar and volcanic) and anthropogenic (e.g., CO₂, sulphate aerosols, and land use)
 48 external radiative forcing. The SSP2-4.5 refers to a scenario combining SSP2-based
 49 socioeconomic and RCP4.5-based energy-emissions-land use scenarios (Eyring et al.,
 50 2016; O'Neill et al., 2016).

51

52

Historical Models				
CAMS-CSM1-0	CAS-ESM2-0	CESM2-FV2	CESM2-WACCM	CESM2
CNRM-CM6-1	CNRM-ESM2-1	CanESM5	E3SM-1-0	E3SM-1-1-ECA
EC-Earth3-Veg-LR	EC-Earth3-Veg	EC-Earth3	EC-Earth3-CC	GFDL-CM4
FGOALS-f3-L	GISS-E2-1-G-CC	GISS-E2-1-G	GISS-E2-1-H	NorESM2-MM
HadGEM3-GC31-MM	INM-CM4-8	INM-CM5-0	IPSL-CM6A-LR	MCM-UA-1-0
MPI-ESM1-2-HAM	MPI-ESM1-2-LR	MRI-ESM2-0	NESM3	NorCPM1
HadGEM3-GC31-LL	NorESM2-LM	GFDL-ESM4	TaiESM1	UKESM1-0-LL
SAM0-UNICON	FIO-ESM-2-0			
SSP2-4.5 Models				
CAMS-CSM1-0	CESM2-WACCM	CESM2	CanESM5	EC-Earth3-Veg
EC-Earth3	FGOALS-f3-L	FIO-ESM-2-0	GFDL-CM4	GFDL-ESM4
GISS-E2-1-G	MPI-ESM1-2-LR	MRI-ESM2-0		

53

54 **Supplementary Notes**

55 **Supplementary Note1: Statistical analysis.**

56 The linear trends are computed using the ordinary least square fit, with the 95%
57 confidence interval for the uncertainty of the trends. For the observational and
58 reanalysis datasets, we show the linear trends during 1960-2010. To compare the
59 changes in observation and CMIP6 models, the linear trends of the observation and
60 historical multi-model mean (MMM) during 1960-2014, and SSP2-4.5 MMM during
61 2015-2100 are presented. For the local spatial standard deviation (SSD) of IAP, we
62 show the linear trends during 1960-2019. The per cent changes of the global ocean
63 inhomogeneity from six observational and reanalysis datasets (IAP, Ishii, EN4.2.0,
64 WOA18, ORAS4, and SODA2.2.4) from 1960 to 2010 are calculated based on their
65 climatological mean state of 1960-1980.

66

67 **Supplementary Note2: Potential spicity.**

68 Potential spicity is a thermodynamic variable whose contours are orthogonal to
69 potential density contours in the potential temperature-salinity space, of which
70 concept has been discussed in many previous publications (e.g., Stommel, 1962;
71 Mamayev, 1975; Veronis, 1972; Munk, 1981; Huang et al., 2018). Previous studies
72 often used the variable potential spiciness (e.g. Munk, 1981), but the contours of the
73 potential spiciness are not strictly orthogonal to those of the potential density. On the
74 other hand, the recently defined potential spicity enforces the orthogonality in the
75 least square sense (Huang et al., 2018). The orthogonality between this variable and
76 potential density suggests that potential spicity provides important thermohaline
77 information independent and supplementary to potential density. Additionally, the
78 potential density and potential spicity are dimensionally homogenous, namely, they
79 share the same unit system kg m^{-3} . Besides, all the calculations of potential density and
80 potential spicity are based on the traditional equation of the state (UNISCO EOS-80), the
81 corresponding potential density and potential spicity calculation is based on the Matlab
82 codes provided by Huang et al. (2018). The detailed definition and calculation of
83 potential spicity can be referred to Huang et al. (2018).

84

85 **Supplementary Note3: the contributions from the temperature and salinity**
86 **changes to the Thermohaline Inhomogeneity (THI) index**

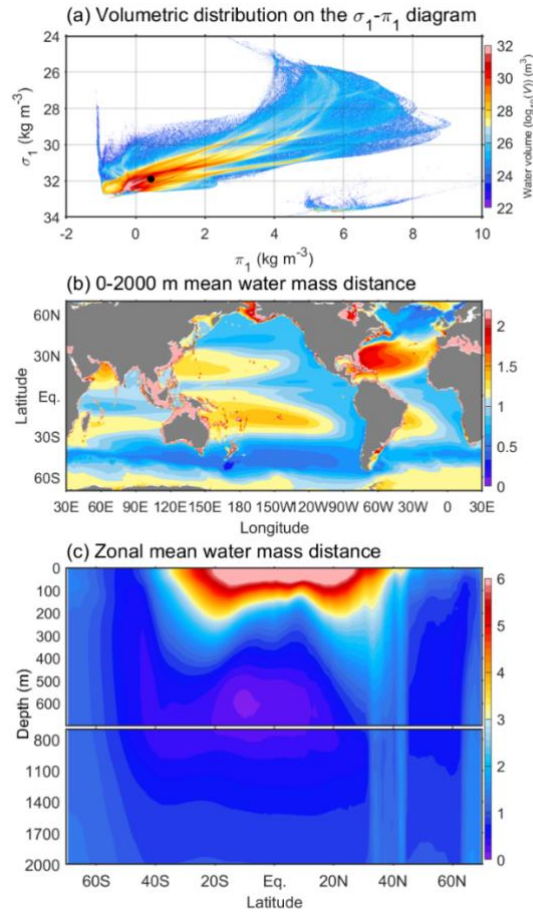
87 The contributions from the temperature and salinity changes to the THI index
88 can be evaluated separately:

89
$$THI_T = THI(\bar{T} + T', \bar{S}), \quad (1)$$

90
$$THI_S = THI(\bar{T}, \bar{S} + S'), \quad (2)$$

91 where THI_T and THI_S represent the THI index change due to the changes in
92 temperature and salinity, respectively (Figure S3). Overbars and primes denote the
93 climatological mean and the temporal deviations from the mean values.
94

95 **Supplementary Figures**



96

97 **Figure S1. (a)** Climatological volumetric distribution of the global water masses in

98 logarithmic scale ($\log_{10}V$, m³) on the potential density-potential spicity (σ_1 - π_1)

99 diagram in 0-2000 m during 1960-2019, with the potential density and potential

100 spicity bin sizes of 0.01 kg m⁻³ and 0.01 kg m⁻³, respectively. The black dot denotes

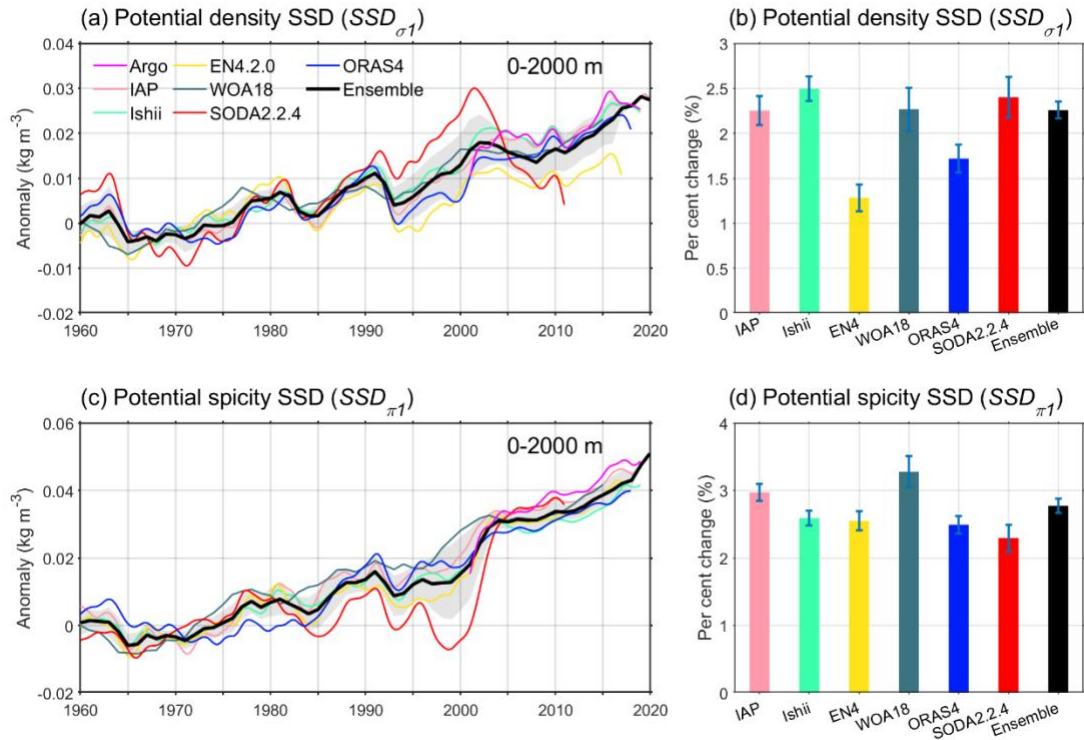
101 the global mean potential density and potential spicity. **(b)** Geographical distribution

102 of 0-2000 m climatological mean water mass distance D (kg m⁻³) during 1960-2019.

103 **(c)** As in **(b)**, but for the meridional-vertical distribution of the zonal-mean water mass

104 distance. Note that the vertical stripe at $\sim 40^\circ\text{N}$ in **(b)** is attributed to the salinity

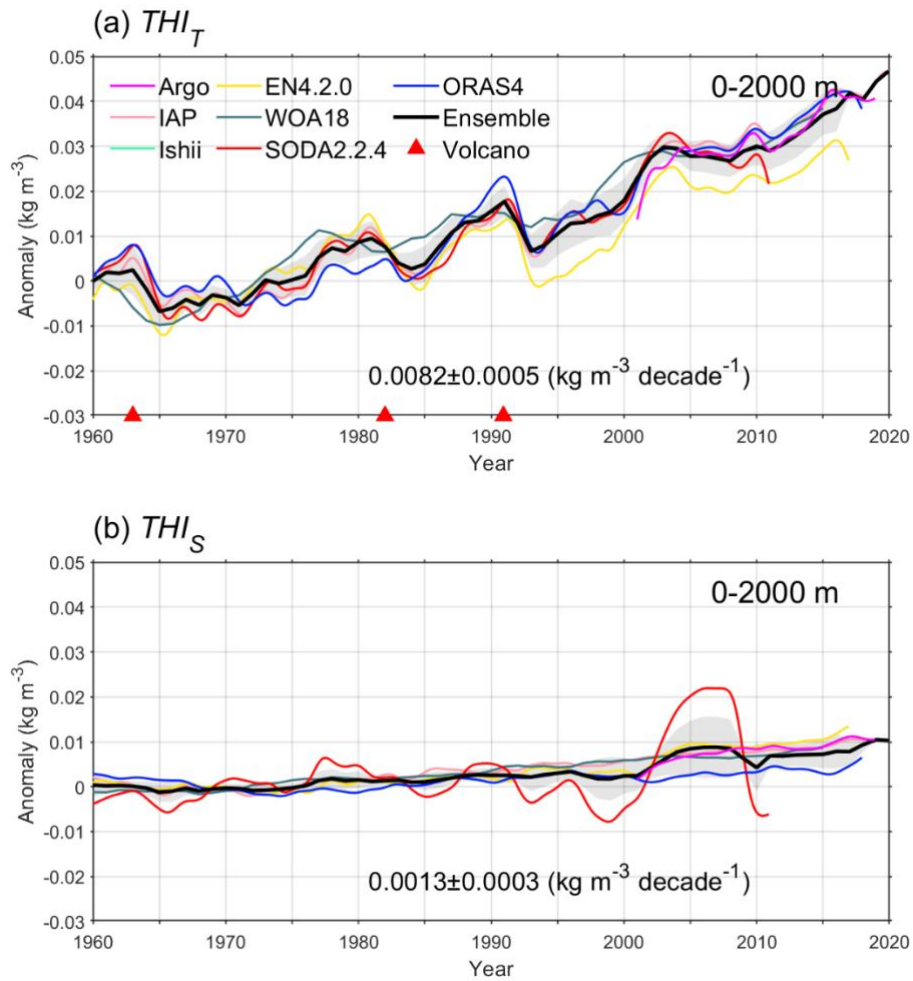
105 structure. All panels are based on IAP data.



106

107 **Figure S2. (a)** Time evolutions of the 3-dimensional volume-weighted spatial
 108 standard deviation (SSD) of global ocean potential density (SSD_{σ_1} ; unit in kg m^{-3}) for
 109 0-2000 m derived from Argo, IAP, Ishii, EN4.2.0, WOA18, SODA2.2.4, and ORAS4.
 110 The black thick curve and the shading denote the ensemble-mean and one standard
 111 deviation range of the 7 datasets, respectively. Here the SSD_{σ_1} is shown as a 2-year
 112 low-pass filtered anomaly relative to the 1960-1980 average baseline (anomaly of
 113 Argo is relative to the 1960-1980 average of IAP). **(b)** Per cent change (%) of 0-2000
 114 m SSD_{σ_1} in 1960-2010 relative to the 1960-1980 average value. The error bars
 115 denote the 95% confidence interval. **(c, d)** are the same as **(a, b)**, but for the potential
 116 spicity SSD (SSD_{π_1} ; unit in kg m^{-3}).

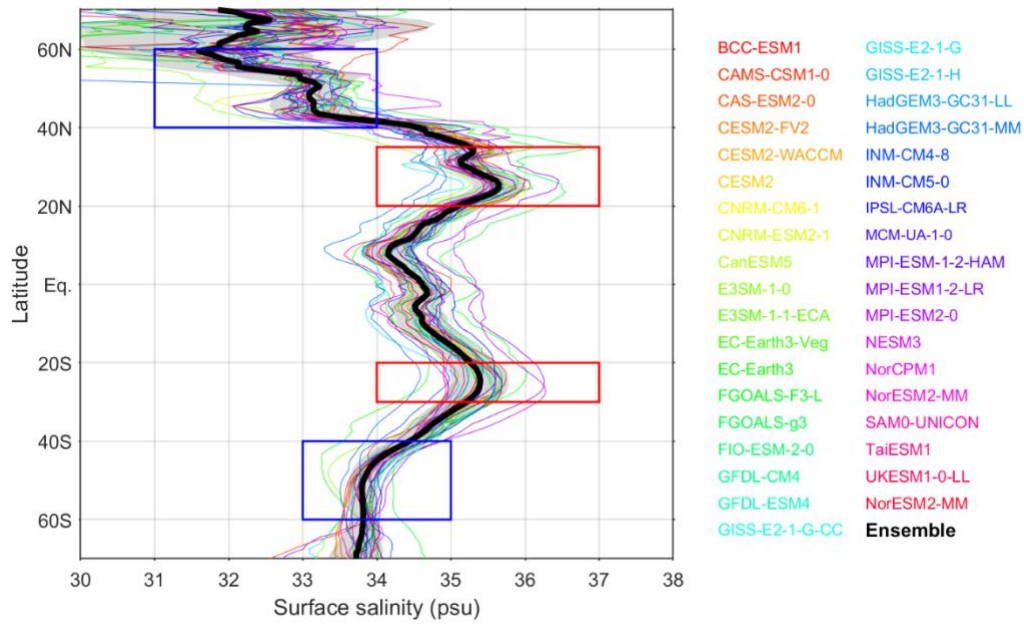
117



118

119 **Figure S3.** Same as **Figure S2a**, but for **(a)** the temperature component of the THI
 120 index (THI_T ; unit in kg m^{-3}) and **(b)** the salinity component of the THI index (THI_S ;
 121 unit in kg m^{-3}) for 0-2000 m. The linear trends for the ensemble mean of the datasets
 122 during 1960-2010 are shown in the lower right corners of each panel. The red
 123 triangles in **a** denote the major volcanic eruptions. See Data and Methods for the
 124 definitions of THI_T and THI_S .

125



126

127 **Figure S4.** Climatological zonal mean surface salinity (psu) derived from 37 CMIP6

128 historical models of 1960-2014. The black thick curve and the grey shading denote

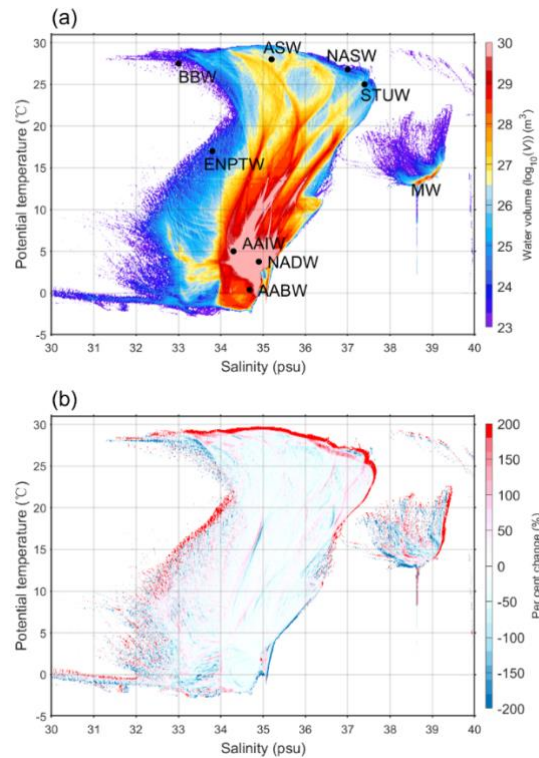
129 the ensemble-mean and one standard deviation range of 37 CMIP6 models,

130 respectively. The red boxes denote the zones (20°N-35°N and 20°S-30°S) with high

131 surface salinity, and the blue boxes present the zones (40°N-60°N and 40°S-60°S)

132 with low surface salinity.

133



134

135 **Figure S5. (a)** climatological volumetric distribution of the global water masses in
 136 logarithmic scale ($\log_{10}V$, m^3) on the potential temperature-salinity (θ - S) diagram for
 137 0-2000 m during 1960-2019, with potential temperature and salinity bin sizes of 0.1°C
 138 and 0.01 psu, respectively. **(b)** As in **(a)**, but for per cent change (%) of the volumes
 139 between 1960-1989 and 1990-2019 relative to the climatological mean of 1960-2019.
 140 At each horizontal grid point, each temperature and salinity profile were first
 141 interpolated into 2 m intervals, so that each 3-dimensional grid cell has a size of $1^\circ \times$
 142 $1^\circ \times 2$ m. Some key water masses are indicated by black solid dots and labeled by the
 143 acronym in **a**, including the Antarctic Bottom Water (AABW), Antarctic Intermediate
 144 Water (AAIW), North Atlantic Deep Water (NADW), Eastern North Pacific
 145 Transition Water (ENPTW), Mediterranean Water (MW), Bay of Bengal Water
 146 (BBW), Arabian Sea Water (ASW), North Atlantic Surface Water (NASW), and
 147 Subtropical Underwater (STUW). All panels are based on IAP data.

148 **References**

149

- 150 Balmaseda, M. A., Mogensen, K., & Weaver, A. T. (2013). Evaluation of the
151 ECMWF ocean reanalysis system ORAS4. *Quarterly Journal of the Royal*
152 *Meteorological Society*, 139(674), 1132-1161.
- 153 Cheng, L. J., Trenberth, K. E., Gruber, N., Abraham, J. P., Fasullo, J. T., Li, G. C., et
154 al. (2020). Improved Estimates of Changes in Upper Ocean Salinity and the
155 Hydrological Cycle. *Journal of Climate*, 33(23), 10357-10381.
- 156 Eyring, V., Bony, S., Meehl, G. A., Senior, C. A., Stevens, B., Stouffer, R. J., &
157 Taylor, K. E. (2016). Overview of the Coupled Model Intercomparison Project
158 Phase 6 (CMIP6) experimental design and organization. *Geoscientific Model*
159 *Development*, 9(5), 1937-1958.
- 160 Ishii, M., Fukuda, Y., Hirahara, S., Yasui, S., Suzuki, T., & Sato, K. (2017). Accuracy
161 of Global Upper Ocean Heat Content Estimation Expected from Present
162 Observational Data Sets. *Sola*, 13, 163-167.
- 163 Good, S. A., Martin, M. J., & Rayner, N. A. (2013). EN4: Quality controlled ocean
164 temperature and salinity profiles and monthly objective analyses with uncertainty
165 estimates. *Journal of Geophysical Research-Oceans*, 118(12), 6704-6716.
- 166 Locarnini, R. A., et al. (2019). World Ocean Atlas 2018, Volume 1: Temperature. A.
167 Mishonov Technical Editor, *NOAA Atlas NESDIS 81*, 52pp.
- 168 O'Neill, B. C., Tebaldi, C., van Vuuren, D. P., Eyring, V., Friedlingstein, P., Hurtt, G.,
169 et al. (2016). The Scenario Model Intercomparison Project (ScenarioMIP) for
170 CMIP6. *Geoscientific Model Development*, 9(9), 3461-3482.

171 Hosoda, S., Suga, T., Shikama, N., & Mizuno, K. (2009). Global Surface Layer
172 Salinity Change Detected by Argo and Its Implication for Hydrological Cycle
173 Intensification. *Journal of Oceanography*, 65(4), 579-586.

174 Huang, R. X., Yu, L. S., & Zhou, S. Q. (2018). New Definition of Potential Spicity by
175 the Least Square Method. *Journal of Geophysical Research-Oceans*, 123(10),
176 7351-7365.

177 Mamayev, O. I. (1975). Temperature-salinity analysis of world ocean waters (p. 384).
178 Amsterdam-Oxford-New York: Elsevier Scientific Publishing Company.

179 Munk, W. (1981). Internal waves and small-scale processes. In *Evolution of physical*
180 *oceanography* (pp. 264–291). Cambridge, MA: MIT Press.

181 Smith, R. D., Dukowicz, J. K., & Malone, R. C. (1992). Parallel Ocean General-
182 Circulation Modeling. *Physica D-Nonlinear Phenomena*, 60(1-4), 38-61.

183 Stommel, H. (1962). On the cause of the temperature-salinity curve in the ocean.
184 National Academy of Science, 48(5), 764–766. [https://doi.org/](https://doi.org/10.1073/pnas.48.5.764)
185 [10.1073/pnas.48.5.764](https://doi.org/10.1073/pnas.48.5.764)

186 Zweng, M. M., et al. (2019). World Ocean Atlas 2018, Volume 2: Salinity. A.
187 *Mishonov Technical Editor, NOAA Atlas NESDIS 82*, 50 pp.

188 Veronis, G. (1972). On properties of seawater defined by temperature, salinity and
189 pressure. *Journal of Marine Research*, 30, 227–255.